Available online at www.sciencedirect.com
ScienceDirect
Earth and Planetary Science Letters 00 (2024) 1–17

SUPPLEMENTAL MATERIAL: The combined effect of heterogeneous thermal conductivity, chemical density contrast, and heat-producing element enrichment on the stability of primordial reservoirs above the core-mantle boundary

J. M. Guerrero[a,*], F. Deschamps[a,*], Wen-Pin Hsieh[a], P. J. Tackley[b]

[a]*Institute of Earth Sciences, Academia Sinica, 128, Sec. 2, Academia Road, Nangang, Taipei 11529, Taiwan*
[b]*Department of Earth Sciences, ETH Zürich, Sonneggstrasse 5, 8092 Zürich, Switzerland*

Contents of the supplemental material

- Text S1 to S2
- Figures S1 to S13

Supplemental material contains Text S1 to S2, which outlines the details of the numerical model and its main characteristics, details regarding converting between potential temperature and full (including the adiabat) temperature, definitions of mantle structures including plume and downwelling regions, and Figures S1 to S13.

1. Text S1 - Details of numerical simulations

We model compressible thermochemical mantle convection using the finite volume code StagYY. The conservation equations of mass, energy, momentum, and composition are solved on a 2D spherical annulus domain [e.g., Hernlund & Tackley, 2008]. Details of the numerical techniques used to solve this system may be found in Tackley [2008]. All simulations are computed non-dimensionally and can be dimensionalized using input and scaling parameters listed in Table S1. Dimensionalizing temperature requires correcting for adiabatic compression effects and is detailed in Text S2. The main properties of our model are discussed below.

*Corresponding Authors: joshua@earth.sinica.edu.tw, frederic@earth.sinica.edu.tw

1.1. Reference thermodynamical model

Compressible thermochemical convection is characterized by variations relative to a thermodynamic reference state (Figure S1). Reference profiles for the density, temperature, and thermal expansivity are calculated based on the thermodynamic relationships for the Earth's mantle, which are summarized in Tackley [1998]. The surface reference temperature, T_{AS}, corresponds to a non-dimensional adiabatic temperature of 0.64 (i.e., a dimensional value of 1600 K). The reference temperature profile represents a geotherm (which corrects for an adiabatic temperature increase) corresponding to T_{AS}. The reference thermal expansivity profile, $\alpha_{\rm ref}(z)$, decreases by a factor of 5 from surface to core-mantle boundary. The density increases with depth by a factor of approximately 1.5. The Grüneisen parameter, γ, varies with depth such that its product with density is constant. Thermal conductivity is calculated separately and the reference conductivity profile depends on the conductivity model employed (see Methods Section in the main text). The parameters defining this reference state is listed in Table S1.

Compressibility generates sinks and sources of heat that are controlled by the dissipation number, Di, which varies radially and is given by

$$\mathrm{Di}(z) = \frac{\alpha_{\rm ref}(z) g D}{C_P}, \tag{S1}$$

where z is the height above the core-mantle boundary (related to the depth coordinate, d, by $d = D - z$ and the radial coordinate, r, by $r = r_{CMB} + z$, where r_{CMB} is the radius of the core-mantle boundary), $\alpha_{\rm ref}(z)$ is the reference thermal expansivity profile, g is the acceleration due to gravity, D is the mantle thickness, and C_P is the heat capacity (which is assumed constant throughout the system). The surface dissipation number is set to $\mathrm{Di}_{Surf} = 1.2$, and the depth variation of thermal expansivity implies a depth average of 0.32.

The fluid properties of the mantle (density, viscosity, thermal diffusivity, and thermal conductivity) are allowed to vary as the system evolves so that the system Rayleigh number is not known *a-priori*. The reference Rayleigh number, $Ra_{\rm ref}$, which governs the vigor of convection, is evaluated using the surface values of thermodynamic parameters and reference viscosity, $\eta_{\rm ref}$. We prescribe $Ra_{\rm ref} = 3 \times 10^8$ for all calculations.

1.2. Viscosity

Viscosity is modeled using an Arrhenius formulation given by

$$\eta_M(\tilde{d}, \tilde{T}, C) = \eta_{\rm ref}[1 + 29H(\tilde{d} - \tilde{d}_{ULM})] \exp\left(V_a \tilde{d} + E_a \frac{1}{\tilde{T} + \tilde{T}_{off}} + \log(\Delta\eta_C) C\right). \tag{S2}$$

Depth- dependence is characterized by a viscosity contrast of 10 across the mantle depth (corresponding to a logarithmic vertical viscosity ratio $V_a = 2.3026$). An additional viscosity jump by a factor of 30 is imposed at the 660-km

boundary (with non-dimensional depth given by $\tilde{d}_{ULM} = 0.22837$) to account for a phase change (expressed by the Heaviside function in Equation (S2)). Temperature- dependence is characterized by a thermal viscosity contrast of 10^7 (corresponding to a logarithmic thermal viscosity ratio $E_a = 16.118$). The parameter $\tilde{T}_{off}$ is a temperature offset, added to the temperature to reduce the viscosity contrast across the top thermal boundary layer. In this study, $\tilde{T}_{off} = 0.90$. A factor of 30 viscosity contrast ($\Delta\eta_C$) is imposed between lower mantle material and thermochemical reservoirs because dense material enriched in bridgmanite [Trampert et al., 2004, Mosca et al., 2012] is assumed to be more viscous [Yamazaki & Karato, 2001].

A yield stress, σ_0, of 290 MPa is imposed at the surface so that the development of a stagnant-lid is avoided. The yield viscosity is defined from the yield stress $\sigma_Y = \sigma_0 + \dot{\sigma}_z P$ and the second invariant of the stress tensor, $\dot{e}$, and is given by

$$\eta_Y = \frac{\sigma_0 + \dot{\sigma}_z P}{2\dot{e}}. \tag{S3}$$

The total viscosity then is given by

$$\eta = \min(\eta_M, \eta_Y) \tag{S4}$$

Finally, viscosity is truncated so that non-dimensional viscosity values do not fall below 10^{-3} or exceed 10^5.

1.3. Phase changes

The transformation of ringwoodite into bridgmanite and ferropericlase at 660 km is modeled with a discontinuous phase transition controlled by defining a point on the phase boundary and a Clapeyron slope, Γ_{660}. Here, the anchor point is set at $d = 660$ km and $T = 1900$ K, and the Clapeyron slope is set to $\Gamma_{660} = -2.5$ MPa K^{-1}. The accompanying density contrast is fixed to $\Delta\rho_{660} = 400$ kg m^{-3} and is scaled with the surface density. Combined with the 660-km viscosity increase (from upper to lower mantle), the 660-km phase change has a strong influence on the geometry of the plumes. This transition acts as a negatively buoyant barrier, which results in a spreading of the plume conduit beneath this boundary, and a thinning above it. Further phase changes in the lowermost mantle from perovskite to post-perovskite is neglected.

2. Text S2 - Derived quantities and statistics on observed physical parameters

2.1. Adiabatic correction and rescaling to Earth's mantle

The energy and momentum equations are solved with the temperature field that has been corrected for adiabatic effects. However, for practical reasons, the output temperature field states are saved as the uncompressed temperature,

which excludes these effects. In all figures that present temperature fields, plume and downwelling contours, or temperature profiles, temperature has been rescaled and corrected with the adiabatic increase of temperature with pressure. The dimensional temperature field, $T(r, \phi)$, is obtained from the non-dimensional, uncompressed temperature field, $\tilde{T}(r, \phi)$, following

$$\Theta(r, \phi) = [\tilde{T}(r, \phi) + \tilde{T}_{top}] \times \Delta T_S \tag{S5}$$

where $\Theta(r, \phi) = T(r, \phi)/a(z)$ is the potential temperature, $\Delta T_S = 2500$ K is the superadiabatic temperature difference, $\tilde{T}_{top}$ is the non-dimensional surface temperature, which is fixed to 0.12 and corresponds to a surface temperature $T_{Surf} = 300$ K, and $a(z)$ is the adiabatic correction at height z above the core-mantle boundary. The adiabatic correction is given by

$$a(z) = \exp\left[\int_0^z \mathrm{Di}_{Surf} \frac{\alpha_{\mathrm{ref}}(z')}{C_{P\mathrm{ref}}(z')} dz'\right] \tag{S6}$$

where Di_{Surf} is the surface dissipation number, and $\alpha_{\mathrm{ref}}(z)$ and $C_{P\mathrm{ref}}(z)$ are the thermodynamic reference thermal expansivity and heat capacity, respectively. The adiabatic correction varies from 1.0 at the surface to about 1.40 at the CMB.

2.2. Definition of mantle structures

Mantle structures, namely thermal upwellings and downwellings, are indicated in the various field snapshots we present in our figures. These structures can be particularly helpful when the field shows no discernible variations that might indicate flow (i.e., a constant or radially varying conductivity field). The contour of an upwelling characterizes mantle plumes and similarly, the contour of a downwelling characterizes subducting slabs. We adapt the definition of thermal structures based on the formalism by Labrosse [2002]. Here, the plume region is defined as regions where the temperature exceeds the horizontally averaged temperature, $\bar{T}(z)$, by a fraction of c_{plume} of the maximum excess temperature anomaly. That is, regions where temperature is given by

$$T_{plume}(z) \geq \bar{T}(z) + c_{plume}[T_{max}(z) - \bar{T}(z)], \tag{S7}$$

where $T_{max}(z)$ is the maximum temperature. Downwelling regions are defined similarly and given by

$$T_{slab}(z) \leq \bar{T}(z) + c_{slab}[T_{min}(z) - \bar{T}(z)], \tag{S8}$$

where $T_{min}(z)$ is the minimum temperature. The values of c_{plume} and c_{slab} are subjective and decreasing these constants increase the regions they characterize. In this study, both c_{plume} and c_{slab} are set to 0.5 so that the regions

are defined by half the magnitude of the difference between the temperature anomaly and the horizontal average.

Thermochemical piles are defined by a threshold value of C. In our calculations, we define thermochemical piles as having C larger than 0.9. The higher threshold value means that piles, as their name suggests, are the densest material that pool on top of the CMB. Even the densest material in our calculations exhibit greater extension above the CMB. Furthermore, a lower threshold value for thermochemical material may result in estimates of the mean pile temperature that are offset by cooler and lighter material.

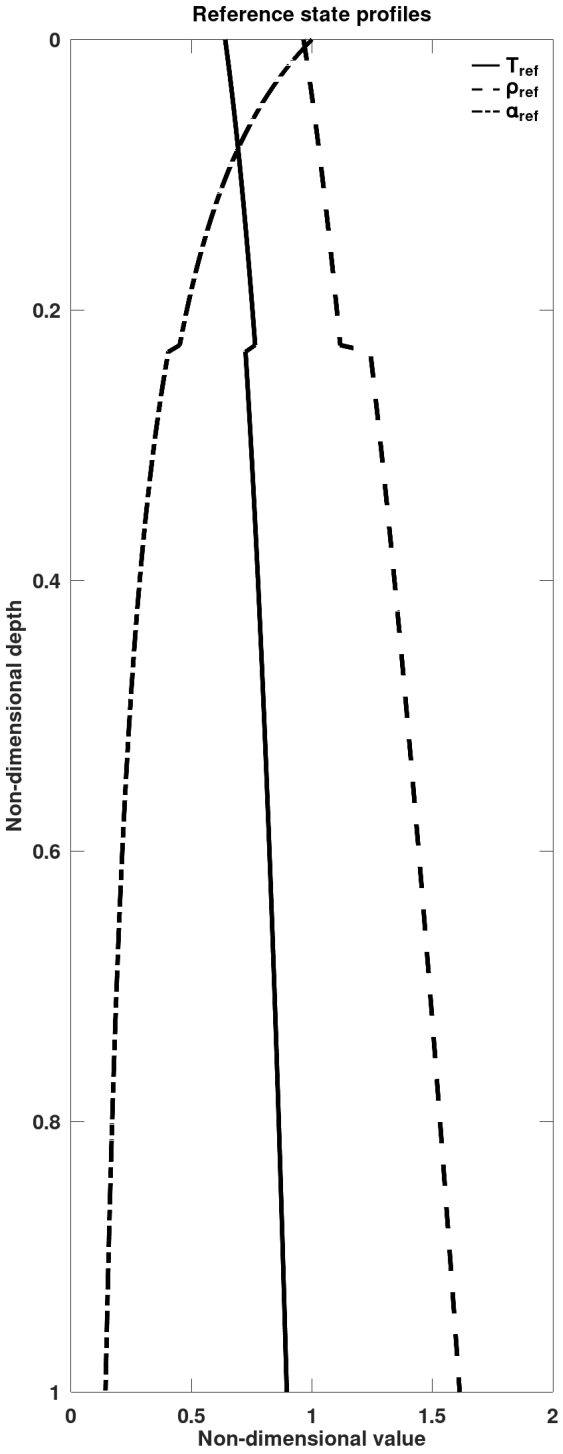

Figure S1: Radial profiles for non-dimensional adiabatic temperature, density, and thermal expansivity indicate the reference state for each calculation. Dimensional values can be found by multiplying by the corresponding surface values.

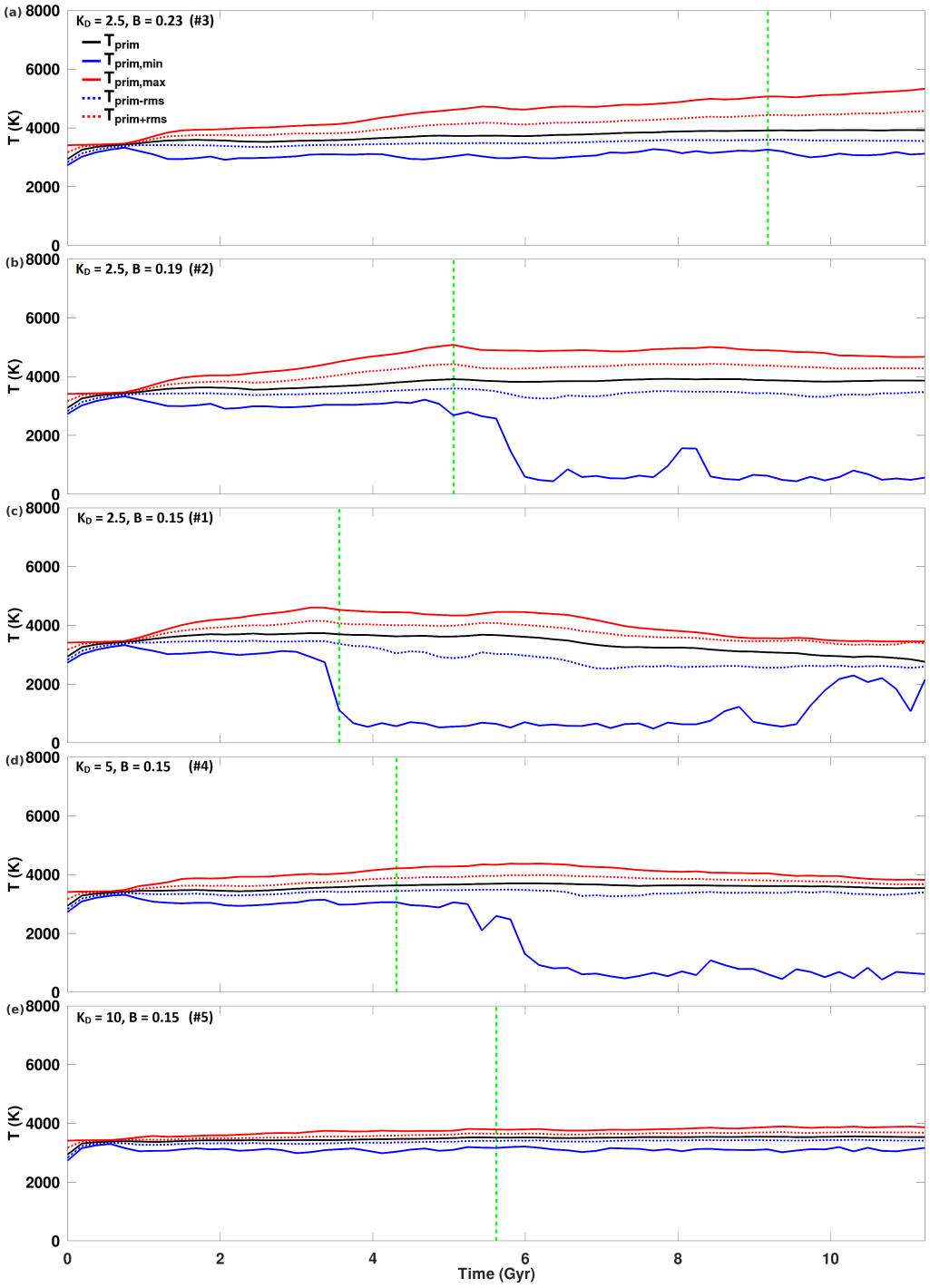

Figure S2: Temperature timeseries for cases presented in Figure 2 in the main text. The dashed-green vertical line indicates the onset of instability in thermochemical reservoirs.

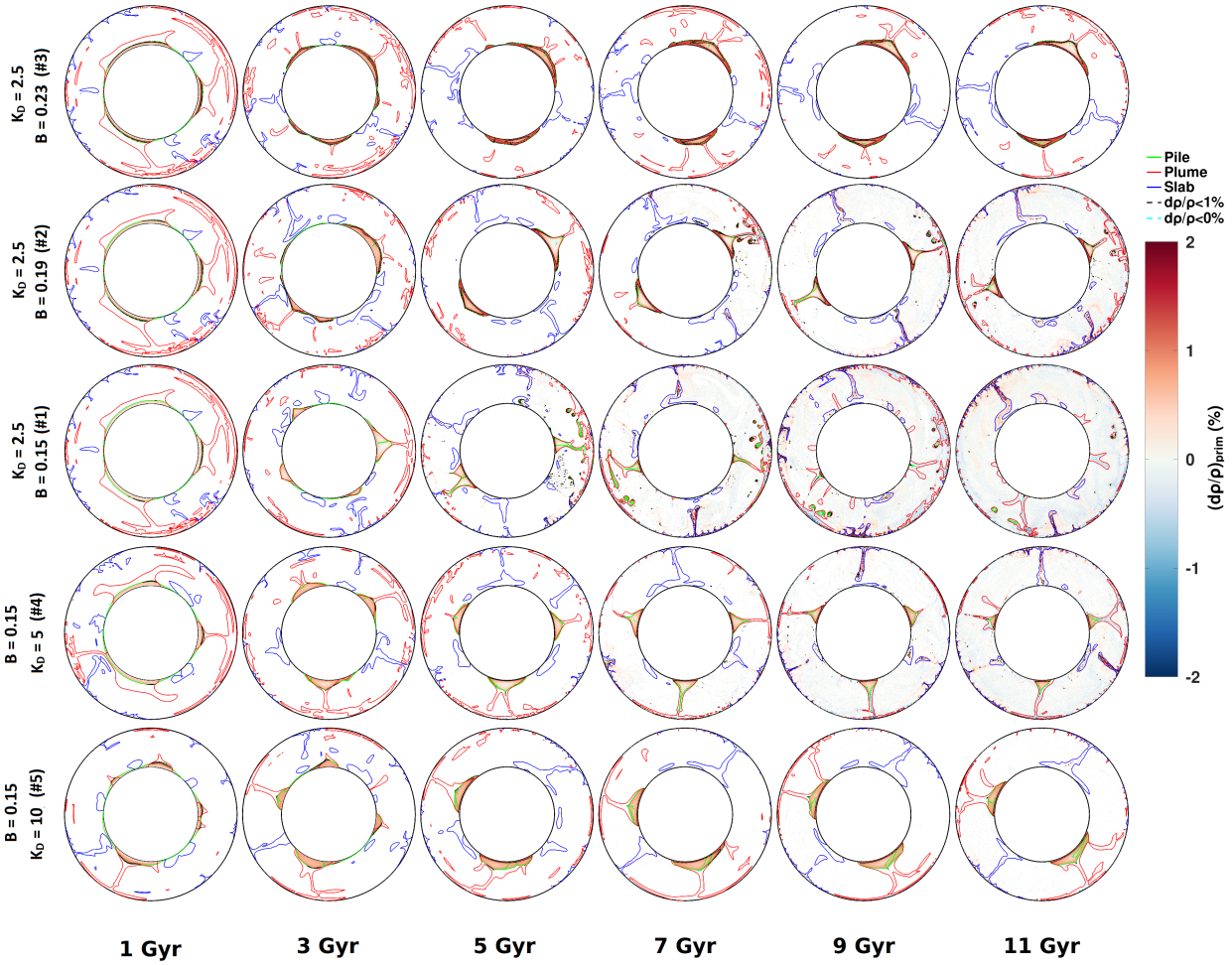

Figure S3: Density anomalies for the primordial field are sampled at 2 Gyr intervals starting at 1 Gyr. These snapshots correspond to cases presented in Figure 1. In the snapshots, solid red contours indicate upwelling regions, solid blue contours indicate downwelling regions, solid green contours indicate primordial material with $C > 0.90$, dashed black contours enclose regions with density anomalies lesser than 1%, and dashed cyan contours enclose regions with density anomalies lesser than 0%.

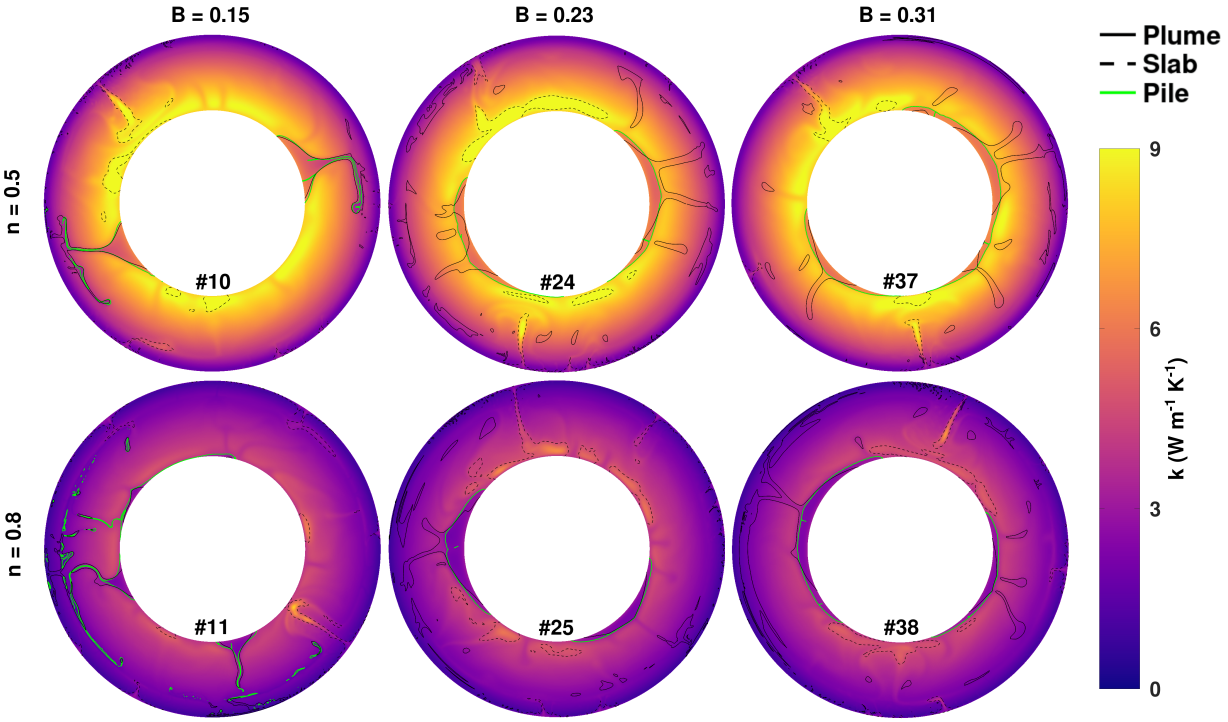

Figure S4: Conductivity field snapshots at t = 4.5 Gyr are illustrated for cases presented in Figure 2. Heat-producing element enrichment is fixed at dH_{prim} = 10 for all cases presented. Plumes are indicated by a solid black contour, slabs are indicated by a dashed black contour, and piles are indicated by a solid green contour. Conductivity corresponds to the values indicated on the colorbar.

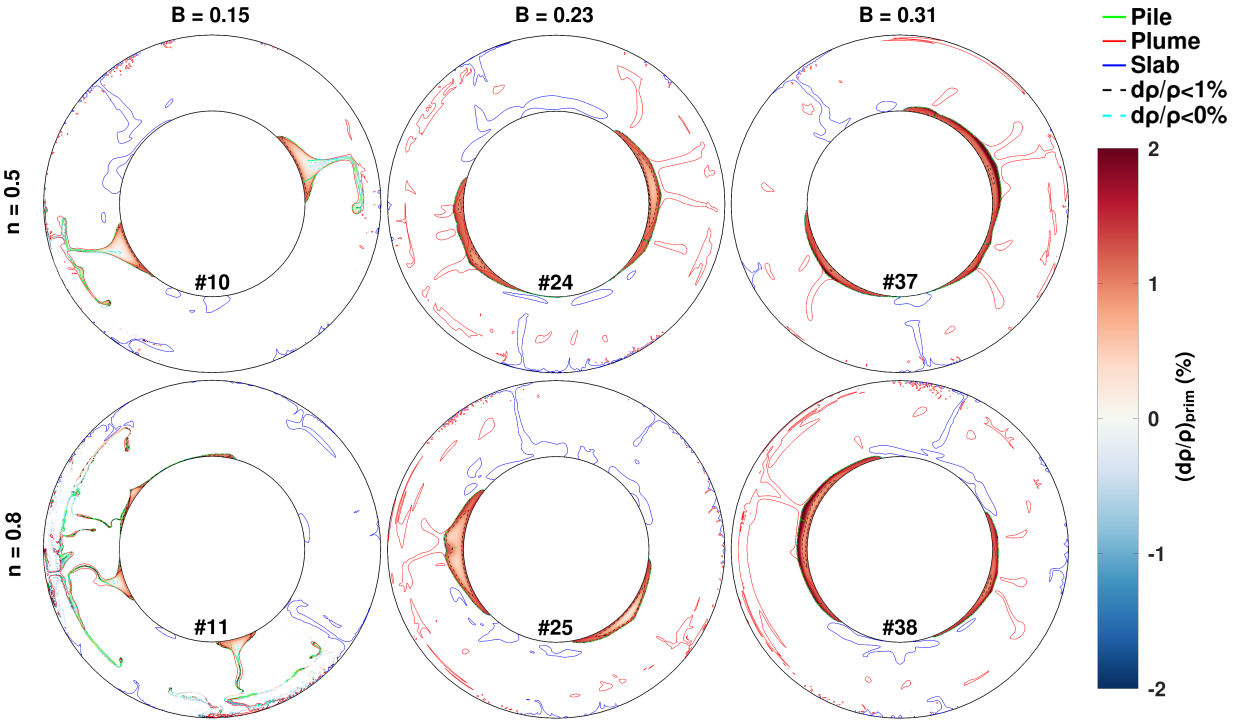

Figure S5: Density anomalies for the primordial field at t = 4.5 Gyr are illustrated for cases presented in Figure 2 and Figure S2. Heat-producing element enrichment is fixed at dH_{prim} = 10 for all cases presented. Contours and colorbar are defined similar to those in Figure S1.

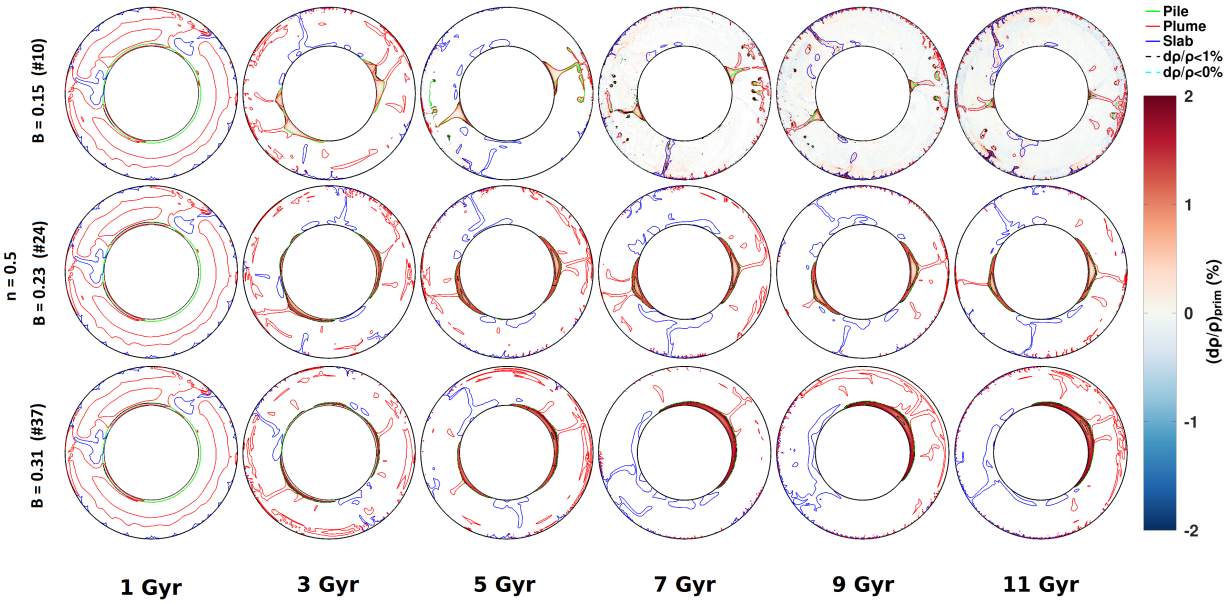

Figure S6: Density anomalies for the primordial field are sampled at 2 Gyr intervals starting at 1 Gyr. These snapshots correspond to cases presented in Figure 2 featuring n = 0.5. Heat-producing element enrichment is fixed at dH_{prim} = 10 for all cases presented. Contours and colorbar are defined similar to those in Figure S1.

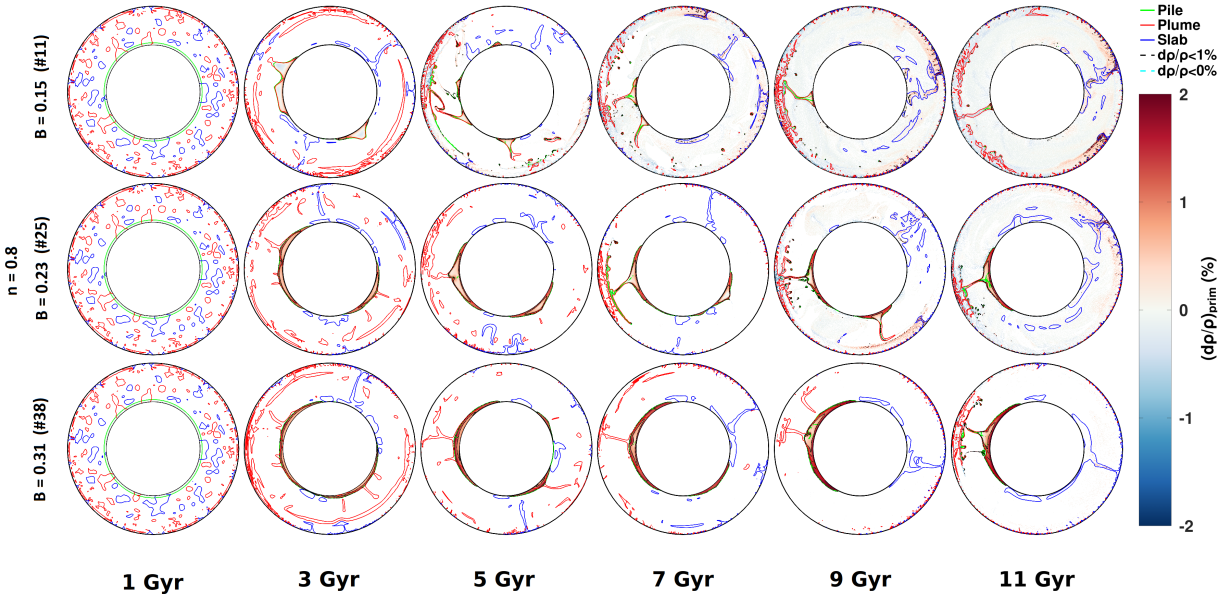

Figure S7: Density anomalies for the primordial field are sampled at 2 Gyr intervals starting at 1 Gyr. These snapshots correspond to cases presented in Figure 2 featuring $n = 0.8$. Heat-producing element enrichment is fixed at $dH_{prim} = 10$ for all cases presented. Contours and colorbar are defined similar to those in Figure S1.

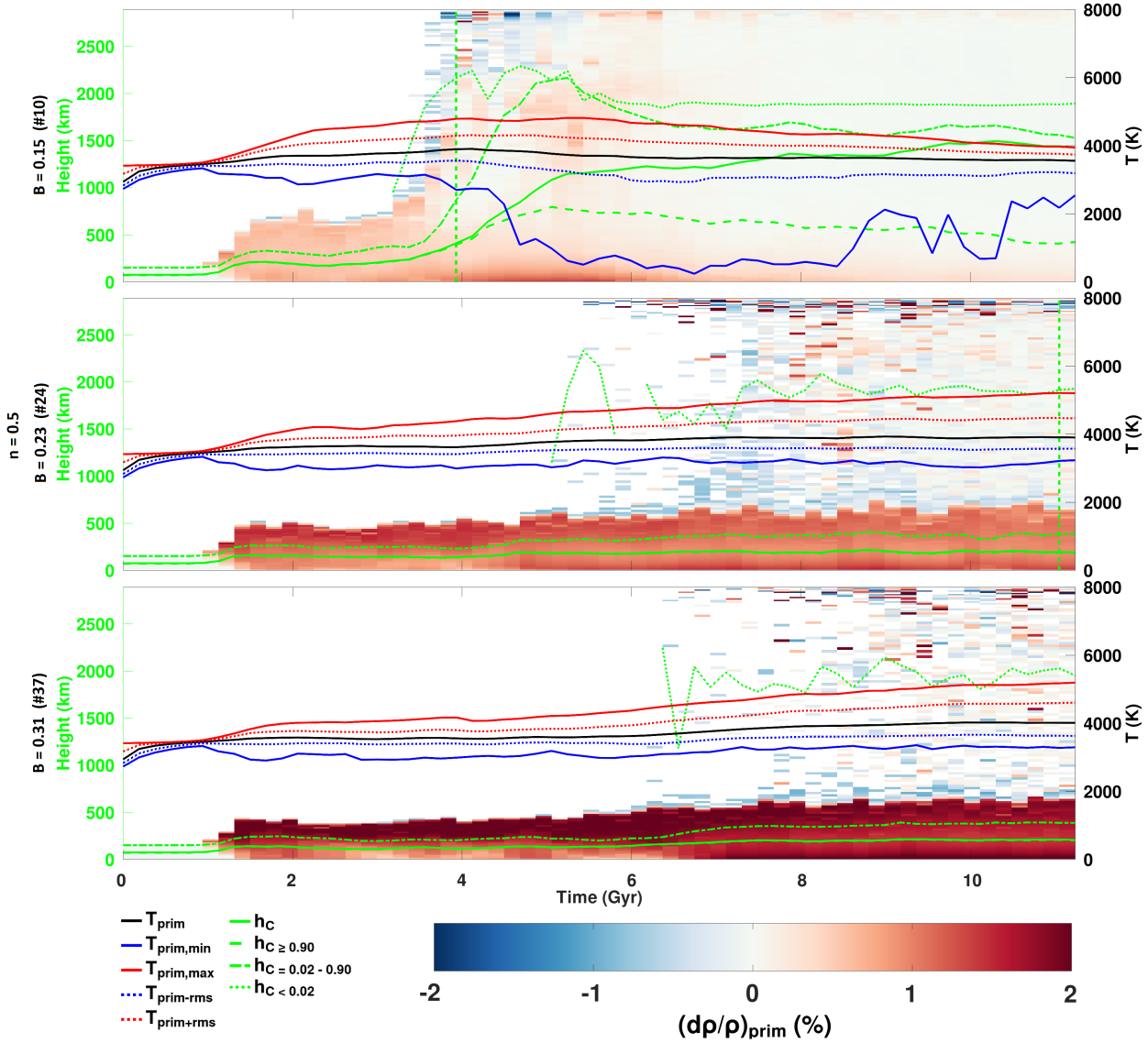

Figure S8: Evolution of the horizontally averaged primordial material density anomalies is illustrated for cases presented in Figure 3 featuring a increasing B for $n = 0.5$. Mean height (corresponding to the left-hand axis scale) and temperature (corresponding to the right-hand axis scale) of primordial material are plotted on top of the density anomaly timeseries. The dashed-green vertical line indicates the onset of instability in thermochemical reservoirs.

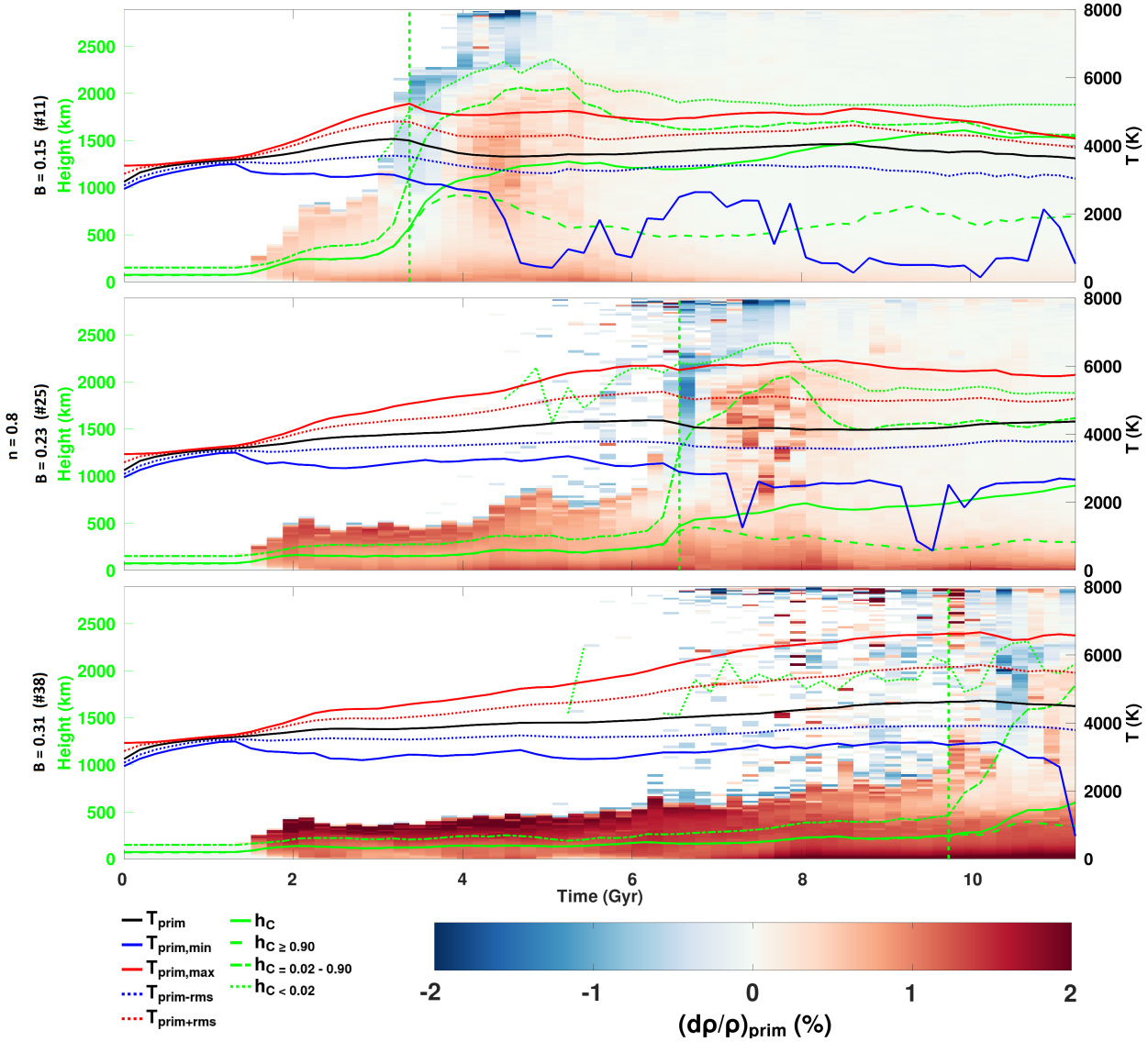

Figure S9: Evolution of the horizontally averaged primordial material density anomalies is illustrated for cases presented in Figure 3 featuring a increasing B for $n = 0.8$. Mean height (corresponding to the left-hand axis scale) and temperature (corresponding to the right-hand axis scale) of primordial material are plotted on top of the density anomaly timeseries. The dashed-green vertical line indicates the onset of instability in thermochemical reservoirs.

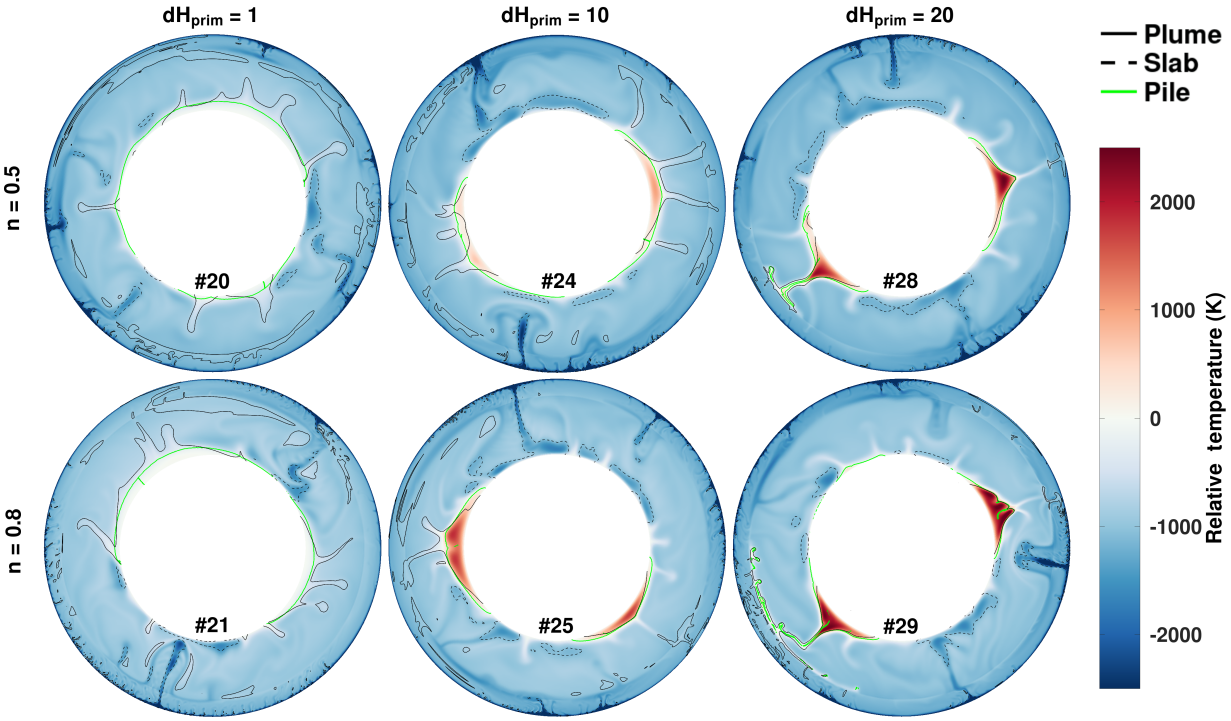

Figure S10: Relative temperature field snapshots at t = 4.5 Gyr are illustrated for cases presented in Figure 3. Buoyancy ratio is fixed at B = 0.23 for all cases presented. Plumes are indicated by a solid black contour, slabs are indicated by a dashed black contour, and piles are indicated by a solid green contour. Relative temperature corresponds to the values indicated on the colorbar.

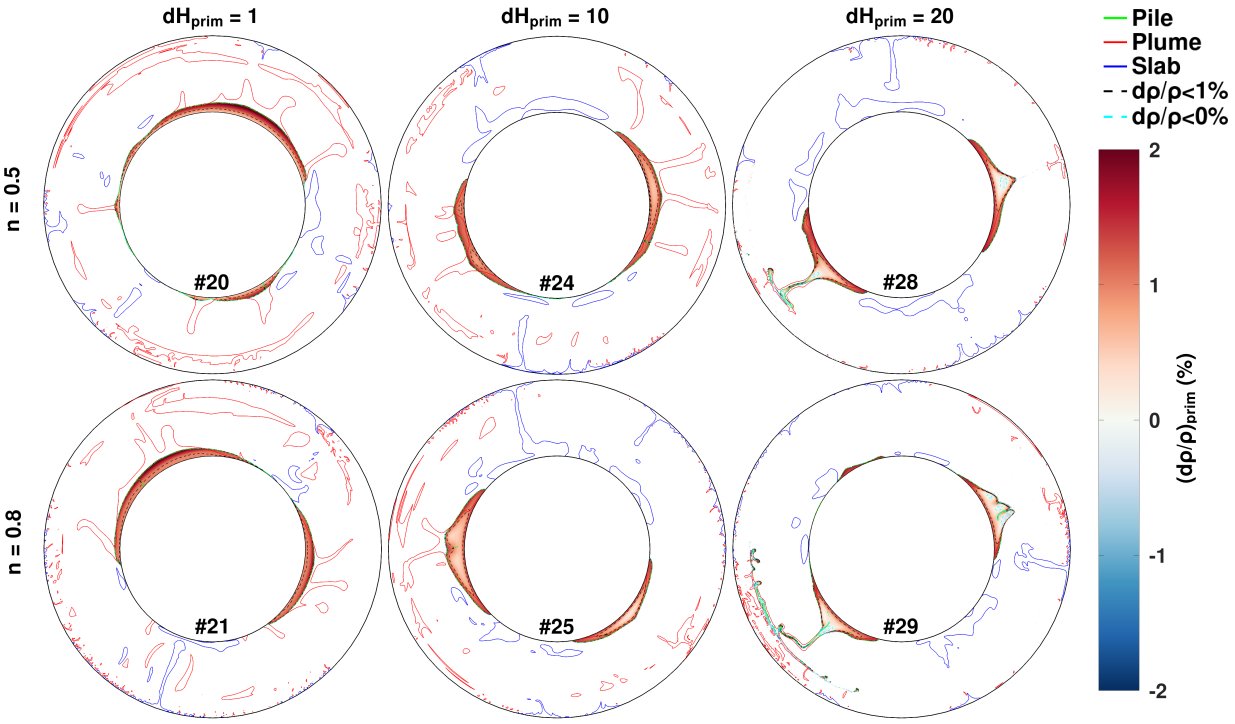

Figure S11: Density anomalies for the primordial field at t = 4.5 Gyr are illustrated for cases presented in Figure 3 and Figure S6. Buoyancy ratio is fixed at B = 0.23 for all cases presented. Contours and colorbar are defined similar to those in Figure S1.

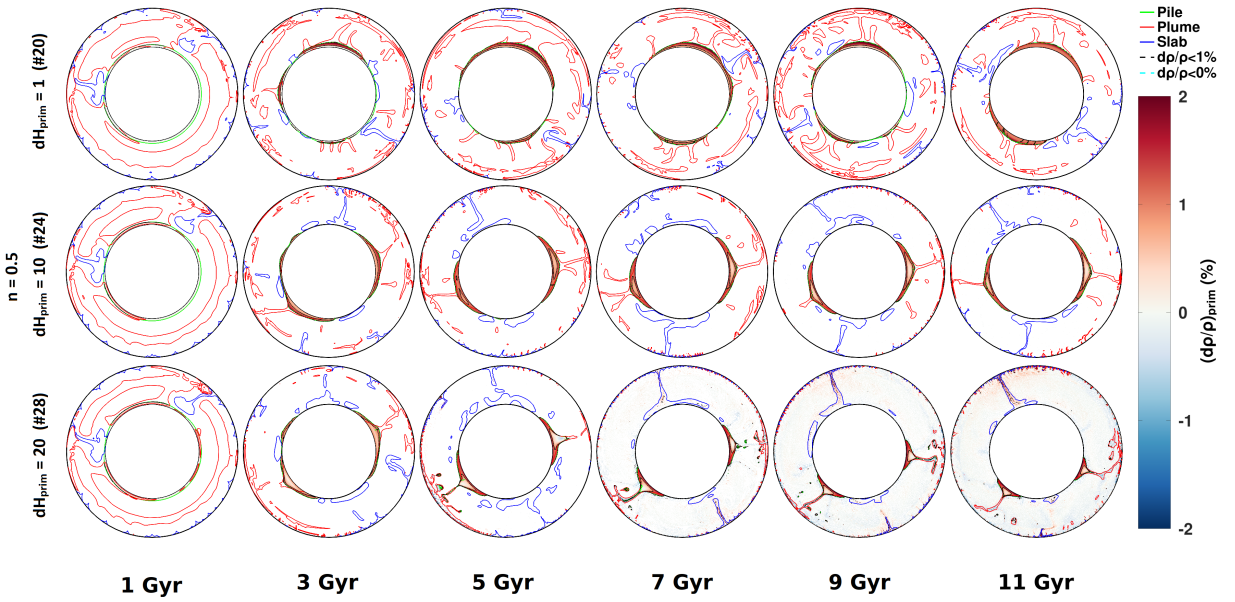

Figure S12: Density anomalies for the primordial field are sampled at 2 Gyr intervals starting at 1 Gyr. These snapshots correspond to cases presented in Figure 3 featuring n = 0.5. Buoyancy ratio is fixed at B = 0.23 for all cases presented. Contours and colorbar are defined similar to those in Figure S1.

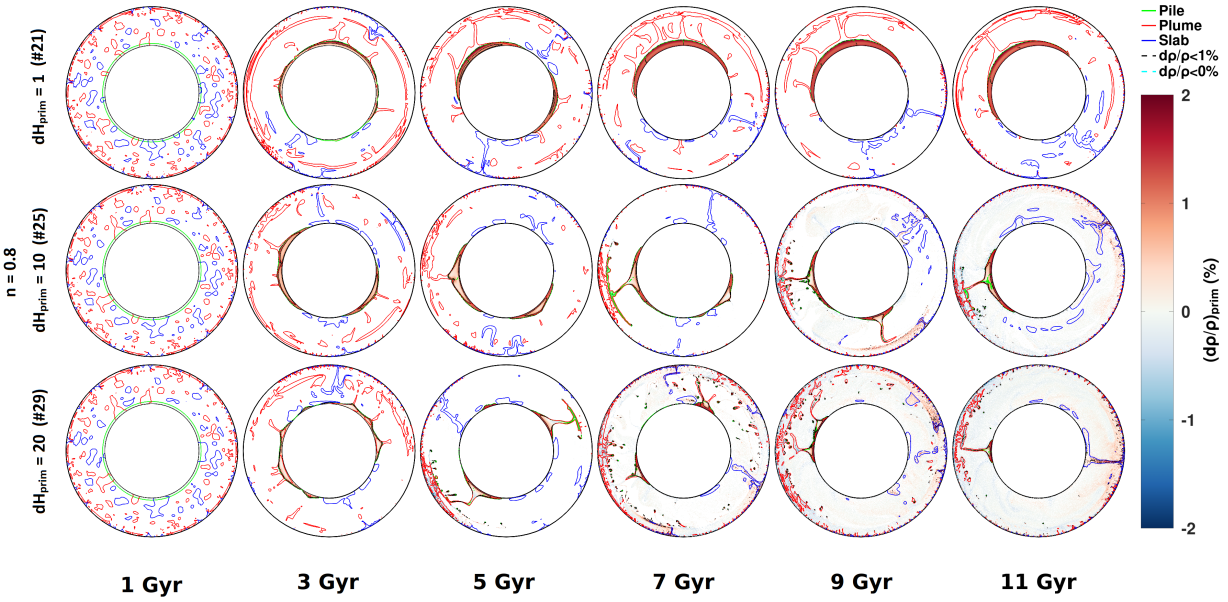

Figure S13: Density anomalies for the primordial field are sampled at 2 Gyr intervals starting at 1 Gyr. These snapshots correspond to cases presented in Figure 3 featuring $n = 0.8$. Buoyancy ratio is fixed at $B = 0.23$ for all cases presented. Contours and colorbar are defined similar to those in Figure S1.

References

Hernlund, J. W., & Tackley, P. J. 2008. Modeling mantle convection in the spherical annulus. Physics of the Earth and Planetary Interiors, 171(1-4), 48-54.

Mosca, I., Cobden, L., Deuss, A., Ritsema, J., & Trampert, J. 2012. Seismic and mineralogical structures of the lower mantle from probabilistic tomography. Journal of Geophysical Research: Solid Earth, 117(B6).

Tackley, P. J. 1998. Three-dimensional simulations of mantle convection with a thermo-chemical basal boundary layer: D. The Core-Mantle Boundary Region, Geodyn. Ser, 28, 231-253.

Tackley, P. J. 2008. Modelling compressible mantle convection with large viscosity contrasts in a three-dimensional spherical shell using the yin-yang grid. Physics of the Earth and Planetary Interiors, 171(1), 7-18.

Trampert, J., Deschamps, F., Resovsky, J., & Yuen, D. 2004. Probabilistic tomography maps chemical heterogeneities throughout the lower mantle. Science, 306(5697), 853-856.

Labrosse, S. 2002. Hotspots, mantle plumes and core heat loss. Earth and Planetary Science Letters, 199(1-2), 147-156.

Yamazaki, D., & Karato, S. I. 2001. Some mineral physics constraints on the rheology and geothermal structure of Earth's lower mantle. American Mineralogist, 86(4), 385-391.